AUT Journal of Mechanical Engineering

AUT J. Mech. Eng., 7(2) (2023) 155-174
DOI: 10.22060/ajme.2023.22109.6054

Large Eddy Simulation and Proper Orthogonal Decomposition Analysis of Two-phase Turbulent Thermomagnetic Convection of a Ferrofluid in a Cubic Cavity

Hossein Abdi, Saber Yekani Motlagh, Hossein Soltanipour*

Department of Mechanical Engineering, Urmia University of Technology (UUT), Urmia, Iran

ABSTRACT: This paper presents the Large-Eddy-Simulation (LES) of two-phase turbulent thermo-magnetic convection of ferrofluid (water- Fe_3O_4) within a cubic cavity. The current two-phase model considers Brownian, thermophoresis, magnetophoresis, and eddy diffusions in the dispersion of ferromagnetic particles. Two parallel electrical wires influence ferrofluid flow. The numerical computations are performed by utilizing the finite volume method for three different magnetic numbers (i.e. $mnf=0$, $mnf=1.4\times10^{10}$ and $mnf=5.6\times10^{10}$). For all numerical calculations, particle volume fraction and Rayleigh are held constant at 0.04 and 10^8 , respectively. Based on the heat transfer analysis, a magnetic field with a strength of $mnf=5.6\times10^{10}$ enhances the Nusselt number by 16.67%. Observed increases in heat transfer can probably be attributed to the Kelvin force induced by the magnetic field, which affects the coherent structures of the flow. Using the Proper Orthogonal Decomposition (POD) method, coherent structures are extracted from velocity and pressure fluctuations. Further, the time coefficients of the first three modes are extracted for the pressure fluctuation. According to the results, the applied magnetic field reduces the cumulative energy of modes and increases the number of modes required to reconstruct a given amount of flow. The coherent structures also change from plane to spanwise roll structures with increasing magnetic numbers. The energy content of the first three modes decreases from 98.7% to 73% as the magnetic field increases from $mnf=0$ to $mnf=1.4\times10^{10}$.

Review History:

Received: Jan. 17, 2023
Revised: Jul. 06, 2023
Accepted: Aug. 15, 2023
Available Online: Sep. 16, 2023

Keywords:

Coherent structure
Large-Eddy Simulation
Magnetic nanofluid
Proper Orthogonal Decomposition
Two-phase flow

1- Introduction

Magnetic nanofluids (ferrofluid) is a colloid of ferromagnetic nanoparticles such as iron, nickel, cobalt, and some of their alloys that are stably dispersed in a carrier liquid such as water, engine oil, or diester. Due to their ability to be strongly magnetized by imposing magnetic fields, ferrofluids are characteristically different from other types of nanofluids. An applied magnetic field can therefore manipulate ferrofluid fluid dynamics and heat transfer rates appropriately. There has been significant interest in magnetic nanofluids due to their unique properties and potential applications, such as heat transfer and thermal management, biomedical engineering, energy harvesting and storage, microfluidics, and so on [1].

The dynamics of ferrofluids under a magnetic field are formulated first by Rosensweig [2]. An analysis of the laminar forced convection of ferrofluid in a rectangular channel was performed by Aminfar et al [3, 4]. According to their results, the magnetic field increases the Nusselt number and friction coefficient. Sheikholeslami and Seyednezhad [5] simulated the natural convection of Fe_3O_4/ ethylene glycol ferrofluid in a porous enclosure. It was shown that the rate of heat transport increases with an increase in magnetic field intensity. A study conducted by Mohammadpourfard et al. [6] examined the effect of magnetic fields on Fe_3O_4-water magnetic nanofluid hydrodynamics and heat transfer specifications. They found that magnetic fields intensify the heat transfer coefficient. Ashwin Kumar et al. [7] investigated the effect of a magnetic field on the velocity and thermal boundary layers of magnetic nanofluids over vertical plates. According to their findings, flow and heat transfer characteristics are affected by the magnetic field. In addition, the nanoparticle volume fraction was found to have a significant impact on the wall friction and heat transfer rate. The effect of a non-uniform magnetic field on a ferrofluid flow in a T-junction was studied by Gerdroodbary et al. [8]. According to their findings, applying a magnetic field increases the average heat transfer coefficient by over 64%. Furthermore, the local heat transfer rate (near the magnetic field) was increased by more than 200%. Khosravi et al. [9] studied a magnetic nanofluid forced convection in the presence of a magnetic field. Based on their findings, Nusselt number and pressure drop increase as nanoparticle volume fraction and magnetic field intensity increase. The effect of a permanent magnet on the thermomagnetic convection of a ferrofluid inside a cavity was reported by Szabo et al. [10]. They identified a condition under which free convection changes to a thermomagnetic one. Javed et al. [11] numerically investigated magnetohydrodynamic impacts

*Corresponding author's email: h.soltanipour@mee.uut.ac.ir

on ferrofluid natural convection inside a square cavity with an obstacle. They found that the rate of convection increases with increasing Rayleigh number and decreases with increasing Hartmann number. The thermomagnetic convection of a ferrofluid inside a vertical annular enclosure was studied experimentally and numerically by Wrobel et al. [12]. It was shown that depending upon the intensity and direction of the magnetic field, the rate of convection can be strengthened or weakened. Lee and Kim [13] numerically determined the role of a magnetic field in ferrofluid heat transfer in cavities containing heat sources with various shapes. According to their simulations, a magnetic field produces vortices that enhance convection heat transfer. The study conducted by Yekani Motlagh et al. [14] investigated natural convection in a titled porous semi-annulus enclosure filled with a ferrofluid. The study demonstrated that increasing the inclination angle of the enclosure leads to a suppression of the heat transfer rate. A numerical analysis of ferrofluid convection inside a curved pipe under a spatially varying magnetic field was presented by Soltanipour et al. [15]. It was found that an applied magnetic field increases heat transfer by approximately 30%.

In a study performed by Banik et al. [16], the focus was on thermomagnetic convection and entropy production in a cubical cavity filled with ferrofluid. The cavity included a cylindrical heat source positioned at its center. The findings of the study revealed that an increase in the strength of the magnetic field resulted in a higher rate of heat transfer. Additionally, the study observed a corresponding increase in entropy generation, indicating a higher degree of irreversibility in the system. In a study conducted by Ayoubi et al. [17], the influence of the strength and position of a magnetic field on the heat transfer rate in an enclosure was investigated. The researchers showed that by placing the magnetic source at the bottom right of the enclosure, a maximum heat transfer enhancement of 11.5% could be achieved. Iftikhar et al. [18] numerically investigated natural convection within a U-shaped cavity filled with water-based ferroparticles under the influence of magneto-hydrodynamic (MHD) effects. The results of their study demonstrated that the presence of ferroparticles in the base fluid (water) led to an augmentation in the heat transfer rate within the enclosure. Conversely, a reversed trend was observed when the Hartmann number was increased.

Shi et al. [19] conducted a study to examine the convective heat transfer and particle distribution within a square cavity when subjected to a magneto-static field. The researchers observed that the introduction of a magnetic field yielded an increase in the Nusselt number, indicating enhanced convective heat transfer. Furthermore, they noted an associated rise in entropy generation due to the presence of the magnetic field. Under uniform magnetic fields, Dixit and Pattamatta [20] examined ferrofluid natural convection in a cubical enclosure. Research results suggested that the direction of a magnetic field can help or suppress natural convection flow.

Nanofluid turbulent convection within enclosures has received very little attention. Goodarzi et al. [21] performed the two-phase mixture modeling of nanofluid mixed convection inside a rectangular shallow enclosure. Increasing the nanofluid volume fraction increased the convection rate for prescribed values of Grashof and Richardson numbers. Magnetic nanofluid convection under the magnetic and buoyancy forces was investigated by Abdi et al. [22]. Using the v2-f turbulence model, they found that as Rayleigh and magnetic numbers increased, the heat transfer rate intensified. Lattice Boltzmann (LB) modeling of nanofluid turbulent free convection was carried out by Sajjadi et al. [23]. Specifically, they found that the particle volume fraction has an augmentative effect on the Nusselt number. Mixed convective heat transfer for pure water and nanofluid in a cubic enclosure containing a rotating adiabatic cylinder was studied by Kareem and Gao [24]. Using a standard k-ε turbulence model, they demonstrated that the rate of heat transfer for nanofluids is considerably higher than that of pure water. Cao et al. [25] investigated the mixed convection of Cu-water nanofluid between two rotating cylinders embedded in a porous medium. The temperature difference between the cylinders triggered free convection, while the rotation of the cylinders resulted in the generation of forced convection. Numerical outcomes indicated that natural convection can be attenuated by the rotation of cylinders. Ghodsinezhad et al. [26] studied the turbulent free convection of Al_2O_3–water nanofluid in a rectangular enclosure. The results showed that the convective heat transfer coefficient reaches its maximum at a nanoparticle volume fraction of 0.1%. The transient turbulent free convection of different water-based nanofluids in a square enclosure was studied by Patel et al. [27]. According to their numerical findings, alumina nanofluid demonstrates superior heat transfer performance compared to other fluids. Recently, Harish and Sivakumar [28] investigated the turbulent free convection of nanofluids in a cubic enclosure. To account for Brownian and thermophoresis diffusions of nanoparticles, they modified the two-phase mixture model. Finite volume simulation coupled with k-ε turbulence model showed that particle fluxes due to Brownian motion enhances convection heat transfer. Harish and Sivakumar [29] examined turbulent mixed convection in vented cubic enclosures for different water-based nanofluids. According to their results, thermophoresis and Brownian diffusion have a greater impact on nanoparticle dispersion in assisting flow conditions.

In turbulent flows, the determination of coherent structures is crucially important since they play a main role in the transport phenomena. The control of turbulence and thereby momentum, heat, and mass transfer phenomena requires the knowledge of coherent structures. The Proper Orthogonal Decomposition (POD) is a robust decomposition technique employed to identify the energetic modes that exhibit correlations within the physical flow field. POD finds widespread application in various thermo-fluidic problems [30, 31].

In Mahapatra's study [32] the structure of buoyancy-driven flow in an enclosure with two discrete heat sources operating alternately was investigated. The Proper Orthogonal

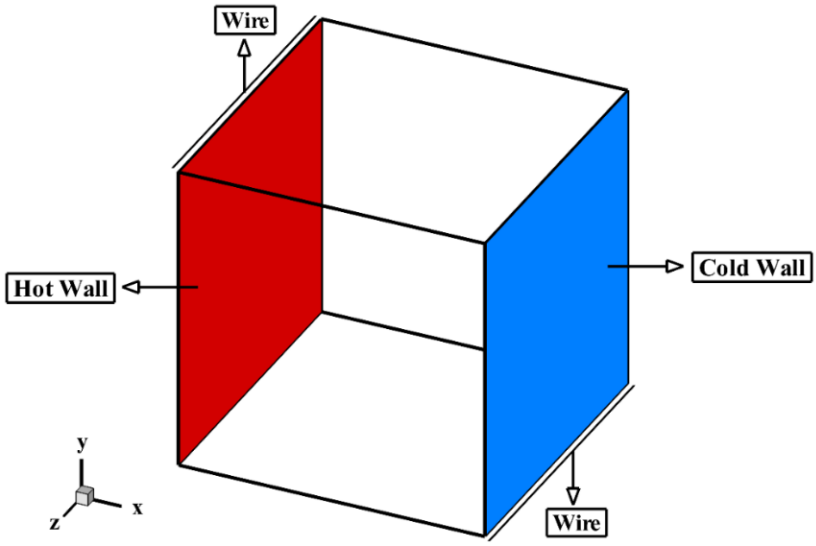

Fig. 1. Representation of the problem

Decomposition (POD) technique was employed to analyze the energy content in different modes and identify the corresponding coherent flow structures for various Rayleigh numbers. The results showed that the first three POD modes accounted for approximately 97% of the total energy content in the flow.

Podvin et al. [33] numerically analyzed the turbulent airflow in a cubic cavity and extracted the coherent structures using the POD method. Their research illustrated that about 60% of the total flow energy belongs to the first 10 modes. Additionally, they found that as the Rayleigh number grows, the size and orientation of coherence structures change considerably. Yekani Motlagh and Taghizadeh [34] extracted coherent structures in a porous cubic cavity using the POD method. They showed that increasing porosity alerts the shape and orientation of coherent structures.

The literature survey indicates that the existing research regarding the nanofluid turbulent convection in enclosures is mostly based on the Reynolds-averaged Navier-Stokes (RANS) equations and single-phase formulation. RANS-based models, such as the *k*-ε and *k*-ω models, primarily focus on predicting the averaged flow properties and turbulence quantities, such as mean velocity and turbulent kinetic energy. However, these models do not capture the intricate characteristics of individual eddies and flow structures in detail. Instead, they provide a representation of the overall behavior of the flow, enabling efficient simulations while sacrificing the resolution of small-scale turbulent features. The application of non-uniform fields undoubtedly influences the turbulent flow structures and can lead to alert in flow and heat transfer characteristics. Therefore, it becomes necessary to model such flows in a manner that is capable of capturing turbulent eddies such as LES or DNS. Additionally, the extraction of coherent structures is of crucial importance for flow control purposes. These coherent structures play a significant role in the overall flow behavior and understanding their dynamics can provide valuable insights for optimizing flow control strategies. To the authors' best knowledge, there is not any study regarding the LES/POD analysis of nanofluids. Therefore, in this paper, the Large-Eddy-Simulation of turbulent thermomagnetic convection of Fe_3O_4 -water ferrofluid in a cubic cavity is performed by a modified two-phase model. The effect of the external magnetic field on the form and energy of coherent structures is determined at different magnetic numbers.

2- Problem statement

A schematic of a cubic cavity having a side length of 0.025m is displayed in Fig. 1. The cavity is filled with Fe_3O_4 /water magnetic nanofluid with the mean particle volume fraction of $\phi_m = 0.04$. The hot and cold walls of the enclosure are at $T_h = 311$ K and $T_c = 309$ K while the top and bottom boundaries are assumed to be perfectly insulated. In addition, the front and back surfaces of the cavity are treated as periodic or cyclic boundary conditions. Turbulent thermomagnetic convection results from buoyancy and magnetic forces which is investigated numerically via a two-phase model. Gravity acts in the negative y-direction. As depicted in Fig. 1, the magnetic nanofluid is subjected to the magnetic fields induced by two parallel electrical wires aligned in the *z*-direction. The normal distance between each electrical wire and adjacent wall is set to $d = 0.005\text{m}$.

Table 1. boundary conditions of cubic cavity with dimensions of $0.025\text{m}\times0.025\text{m}\times0.025\text{m}$

	Hot Wall (Left Wall)	Cold Wall (Right wall)	Up Wall	Down Wall	Front and Back
Temperature	$T_h = 311\ \text{K}$	$T_c = 309\ \text{K}$	$\frac{\partial T}{\partial n}=0$	$\frac{\partial T}{\partial n}=0$	periodic
Velocity	$u=v=w=0$	$u=v=w=0$	$u=v=w=0$	$u=v=w=0$	periodic
Volume fraction	$\frac{\partial \phi}{\partial x}=-\frac{D_T}{D_B}\frac{\partial T}{\partial x}+\frac{\phi}{\mathbf{H}}\xi L(\xi)\frac{\partial \mathbf{H}}{\partial x}$	$\frac{\partial \phi}{\partial x}=-\frac{D_T}{D_B}\frac{\partial T}{\partial x}+\frac{\phi}{\mathbf{H}}\xi L(\xi)\frac{\partial \mathbf{H}}{\partial x}$	$\frac{\partial \phi}{\partial y}=\frac{\phi}{\mathbf{H}}\xi L(\xi)\frac{\partial \mathbf{H}}{\partial y}$	$\frac{\partial \phi}{\partial y}=\frac{\phi}{\mathbf{H}}\xi L(\xi)\frac{\partial \mathbf{H}}{\partial y}$	periodic
Pressure	$\frac{\partial p}{\partial x}=0$	$\frac{\partial p}{\partial x}=0$	$\frac{\partial p}{\partial y}=0$	$\frac{\partial p}{\partial y}=0$	periodic

The components and magnitude of the magnetic field intensity vector are given by [35]:

$$H_x=\frac{-I}{2\pi}\left(\sum_i \frac{y-b_i}{(x-a_i)^2+(y-b_i)^2}\right) \quad (1)$$

$$H_y=\frac{I}{2\pi}\left(\sum_i \frac{x-a_i}{(x-a_i)^2+(y-b_i)^2}\right) \quad (2)$$

$$H=\sqrt{H_x^2+H_y^2} \quad (3)$$

where (a_i,b_i) refers to the coordinates of the *i*-th wire and I is the electrical current.

Langevin approximation is used to compute the magnetization of magnetic nanofluid [36]:

$$M=M_s L(\zeta) \quad (4)$$

where $\zeta=\frac{m_p\mu_0 H}{k_B T}$ is the Langevin argument, $L(\zeta)=\coth(\zeta)-1/\zeta$, $M_s=\frac{6\phi}{\pi d_p^3}m_p$ is the saturation magnetization and $m_p=\frac{4\mu_B\pi d_p^3}{6\times91.25\times10^{-30}}$ stands for the magnetic moment of ferromagnetic nanoparticles [2].

2- 1- Governing equations

Ferrofluid flow in the cavity is supposed to be three-dimensional, unsteady, incompressible, two-phase, and turbulent. Impacts of viscous dissipation, thermal radiation, and compression work are neglected from the energy equation. The Boussinesq approach is utilized to approximate the density variation in the buoyant force. The differential equations describing the ferrofluid motion are as follows [35-37]:

$$\nabla.(\rho_{nf}\vec{\mathbf{V}})=0 \quad (5)$$

$$\rho_{nf}\frac{D\vec{\mathbf{V}}}{Dt}=-\nabla p+\nabla.\left[(\mu_{nf}+\mu_t)\nabla\vec{\mathbf{V}}\right]+\mu_0 M.\nabla\vec{\mathbf{H}}-(\rho\beta)_{nf}\,g\,(T-T_c)\hat{\mathbf{n}}_g \quad (6)$$

$$(\rho c_p)_{nf}\frac{DT}{Dt}=\nabla.\left[(k_{nf}+k_t)\nabla T\right]-\rho_p c_{p,p}\left[D_B\nabla\phi+D_t\nabla\phi+D_T\nabla T-D_B\frac{\phi}{\vec{\mathbf{H}}}\zeta.L(\zeta)\nabla(|\vec{\mathbf{H}}|)\right].\nabla T-\mu_0 T\frac{\partial M}{\partial T}(\vec{\mathbf{V}}.\nabla(|\vec{\mathbf{H}}|)) \quad (7)$$

$$\frac{D\phi}{Dt}=\nabla.(D_B\nabla\phi)+\nabla.(D_T\nabla T)+\nabla.(D_t\nabla\phi)-\nabla.(D_B\frac{\phi}{|\mathbf{H}|}\zeta.L(\zeta)\nabla(|\mathbf{H}|)) \quad (8)$$

where $\mathbf{V}$, *p, and T* refer to velocity, pressure, and temperature, respectively. Also, $\mu_0=4\pi\times10^{-7}\,\text{T.m/A}$ represents the permeability of the vacuum, μ_t denotes the turbulent viscosity, $\hat{\mathbf{n}}_g$ is the unit vector of gravitational acceleration, $k_t=\frac{\mu_t.c_{nf}}{Pr_t}$ stands for the turbulent thermal conductivity, and $Pr_t=1$ is the turbulent Prandtl number. Besides, the terms $\mu_0 M.\nabla\mathbf{H}$ and $-\mu_0 T\frac{\partial M}{\partial T}(\mathbf{V}.\nabla(|\mathbf{H}|))$ in the momentum and energy equations represent the Kelvin body force and magneto-

caloric effect [36]. The volume fraction of nanoparticles (ϕ) refers to the ratio of the volume occupied by the nanoparticles to the total volume of the system. The first, second, third, and fourth terms on the right-hand side of Eq. (8) denote the flux of particles due to Brownian, thermophoresis, turbulent eddy diffusion, and magnetophoresis effects, respectively [37-39].

In this study, the thermophoresis, Brownian, and turbulent eddy diffusion factors are given by[37]:

$$D_T = 0.26\left(\frac{k_f}{2k_f+k_p}\right)\left(\frac{\mu_f\phi}{T}\right), D_B = \frac{k_B T}{3\pi\mu_f d_p}, D_t = \frac{\mu_t}{\rho_{nf} Sc_t} \tag{9}$$

where d_p represents the diameter of the nanoparticle and its value is 4nm. Moreover, $k_B = 1.38065\times10^{-23}$ J/K is the Boltzmann constant and $Sc_t = 1$ indicates the turbulent Schmidt number.

2- 2- Smagorinsky model

The well-known Smagorinsky turbulence model is used in this study. In the Smagorinsky model, the turbulent viscosity is obtained from [40]:

$$\mu_t = \rho_{nf} L_{ss}^2 \left|\bar{S}\right| \tag{10}$$

where $|\bar{S}| = (2\bar{S}_{ij}\bar{S}_{ij})^{1/2}$, $\bar{S}_{ij} = \frac{1}{2}(\frac{\partial \bar{u}_i}{\partial x_j} + \frac{\partial \bar{u}_j}{\partial x_i})$ is the rate-of-strain tensor and L_{ss} is the mixing length of subgrid scales. Also, L_{ss} is computed from:

$$L_{ss} = \min(\kappa d, C_s \forall^{1/3}) \tag{11}$$

where $\forall = (\Delta x \Delta y \Delta z)^{1/3}$ is the volume of the computational mesh, κ is the von Karman constant and d denotes the distance to the nearest wall.

2- 3- Nondimensionalization

The following bold variables are employed in the nondimensionalization process [41, 42]:

$$\boldsymbol{t} = \frac{v_f t}{L^2}, \boldsymbol{(x,y)} = \frac{(x,y)}{L}, \boldsymbol{p} = \frac{pL^2}{\rho_f v_f^2}, \mathbf{H} = \frac{\vec{\mathbf{H}}}{H_0}, \mathbf{V} = \frac{\vec{\mathbf{V}} L}{v_f}, \boldsymbol{\nabla} = \nabla L, \boldsymbol{M} = \frac{M}{M_0}, \boldsymbol{T} = \frac{T-T_c}{T_h-T_c}, \boldsymbol{\phi} = \frac{\phi}{\phi_m}, \boldsymbol{D_B} = D_B / D_{B0}, \boldsymbol{D_T} = D_T / D_{T0}$$

With $H_0 = \frac{I}{2\pi d}$, $M_0 = M(H_0, T_c, \phi_m)$, $D_{B0} = D_B(T_c)$ and $D_{T0} = D_T(T_c, \phi_m)$.

Accordingly, the final nondimensional version of governing equations becomes as

$$\boldsymbol{\nabla}.((\frac{\rho_{nf}}{\rho_f})\mathbf{V}) = 0 \tag{12}$$

$$(\frac{\rho_{nf}}{\rho_f})\frac{D\mathbf{V}}{Dt} = -\boldsymbol{\nabla p} + \boldsymbol{\nabla}.\left[\frac{(\mu_{nf}+\mu_t)}{\mu_f}\nabla\mathbf{V}\right] + (mnf)\mathbf{H}.\nabla|\mathbf{H}| - \frac{(\rho\beta)_{nf}}{(\rho\beta)_f}\frac{Ra}{Pr}\boldsymbol{T}\hat{\mathbf{n}}_g \tag{13}$$

$$\frac{(\rho c_p)_{nf}}{(\rho c_p)_f}\frac{D\boldsymbol{T}}{Dt} = \boldsymbol{\nabla}.\left[(\frac{1}{Pr}(\frac{k_{nf}}{k_f}) + \frac{1}{Pr_t}(\frac{\mu_t}{\mu_f})(\frac{c_{p,nf}}{c_{p,f}}))\boldsymbol{\nabla T}\right] - \frac{1}{Le}\frac{1}{Pr}\left[\boldsymbol{D_B}\boldsymbol{\nabla\phi} + (\frac{\mu_t}{\mu_f})(\frac{\rho_f}{\rho_{nf}})(\frac{Sc}{Sc_t})\boldsymbol{D_t}\boldsymbol{\nabla\phi} + (\frac{1}{R_{BT}})\boldsymbol{D_T}\boldsymbol{\nabla T} - \boldsymbol{D_B}\frac{\boldsymbol{\phi}}{|\mathbf{H}|}\zeta.L(\zeta)\nabla(|\mathbf{H}|)\right].\boldsymbol{\nabla T} - (mnf)Ec(\boldsymbol{T}+\delta_T)\frac{\partial \boldsymbol{M}}{\partial \boldsymbol{T}}(\mathbf{V}.\nabla(|\mathbf{H}|)) \tag{14}$$

$$\frac{D\boldsymbol{\phi}}{Dt} = \frac{1}{Sc}[\boldsymbol{\nabla}.(\boldsymbol{D_B}\boldsymbol{\nabla\phi}) + \frac{Sc}{Sc_t}\boldsymbol{\nabla}.\left(\boldsymbol{D_t}(\frac{\mu_t}{\mu_f})(\frac{\rho_f}{\rho_{nf}})\boldsymbol{\nabla\phi}\right) + (\frac{1}{R_{BT}})\boldsymbol{\nabla}.(\boldsymbol{D_T}\boldsymbol{\nabla T})) - \boldsymbol{\nabla}.\left(\boldsymbol{D_B}\frac{\boldsymbol{\phi}}{|\mathbf{H}|}\zeta.L(\zeta)\boldsymbol{\nabla}(|\mathbf{H}|)\right)] \tag{15}$$

The important non-dimensional numbers in Eq. (12-14) are magnetic number ($mnf = \frac{\mu_0 M_0 H_0 L^2}{\rho_f v_f^2}$), Prandtl number ($Pr = \frac{\mu_f c_f}{k_f}$), Rayleigh number ($Ra = \frac{g\beta_f \Delta T L^3}{v_f \alpha_f}$), the ratio of Brownian to thermophoretic diffusivities ($R_{BT} = \frac{\phi_m D_{B0} T_c}{D_{T0}(T_h - T_c)}$), Lewis number ($Le = \frac{k_f}{\rho_p c_p D_{B0} \phi_m}$), Eckert number ($Ec = \frac{v_f^2}{c_p L^2 (T_h - T_c)}$) and non-dimensional temperature difference ($\delta_T = \frac{T_c}{T_h - T_c}$).

Boundary and initial conditions to be imposed in Eq. (12-14) are as follows:

Cold wall:

$$\boldsymbol{V} = \boldsymbol{T} = \frac{\partial \boldsymbol{p}}{\partial \boldsymbol{x}} = 0, \frac{\partial \boldsymbol{\phi}}{\partial \boldsymbol{x}} = -\frac{D_T}{D_B}\frac{\partial \boldsymbol{T}}{\partial \boldsymbol{x}} + \frac{\boldsymbol{\phi}}{\boldsymbol{H}}\zeta.L(\zeta)\frac{\partial \boldsymbol{H}}{\partial \boldsymbol{x}}$$

Hot wall:

$$\boldsymbol{T} = 1, \boldsymbol{V} = \frac{\partial \boldsymbol{p}}{\partial \boldsymbol{x}} = 0, \frac{\partial \boldsymbol{\phi}}{\partial \boldsymbol{x}} = -\frac{D_T}{D_B}\frac{\partial \boldsymbol{T}}{\partial \boldsymbol{x}} + \frac{\boldsymbol{\phi}}{\boldsymbol{H}}\zeta.L(\zeta)\frac{\partial \boldsymbol{H}}{\partial \boldsymbol{x}}$$

Upper and bottom walls:

$$\boldsymbol{V} = \frac{\partial \boldsymbol{p}}{\partial \boldsymbol{x}} = 0, \frac{\partial \boldsymbol{\phi}}{\partial \boldsymbol{y}} = \frac{\boldsymbol{\phi}}{\boldsymbol{H}}\zeta.L(\zeta)\frac{\partial \boldsymbol{H}}{\partial \boldsymbol{y}}$$

As mentioned earlier, on the back and front surfaces, periodic boundary conditions are applied. The initial conditions for the problem are as follows:

$$\boldsymbol{V(x,y,z,0) = p(x,y,z,0) = 0, T(x,y,z,0)} = 1/2, \boldsymbol{\phi(x,y,z,0)} = 1$$

Moreover, the average Nusselt number on the hot and cold walls can be calculated as:

$$Nu_{Avg} = -\iint \frac{k_{nf}}{k_f}\frac{\partial \boldsymbol{T}}{\partial \boldsymbol{x}}\boldsymbol{dydz} \tag{16}$$

Table 2. Thermophysical properties of water and magnetite [4]

phase	d(nm)	$\mu\times10^{-6}(\frac{\text{kg}}{\text{m.s}})$	$\beta\times10^{-5}(\frac{1}{\text{K}})$	$c_p(\frac{\text{J}}{\text{kg.K}})$	$k(\frac{\text{W}}{\text{m.K}})$	$\rho(\frac{\text{kg}}{\text{m}^3})$
Water	0.384	695	36.2	4178	0.628	993
Fe_3O_4	4	-	1.3	670	6	5200

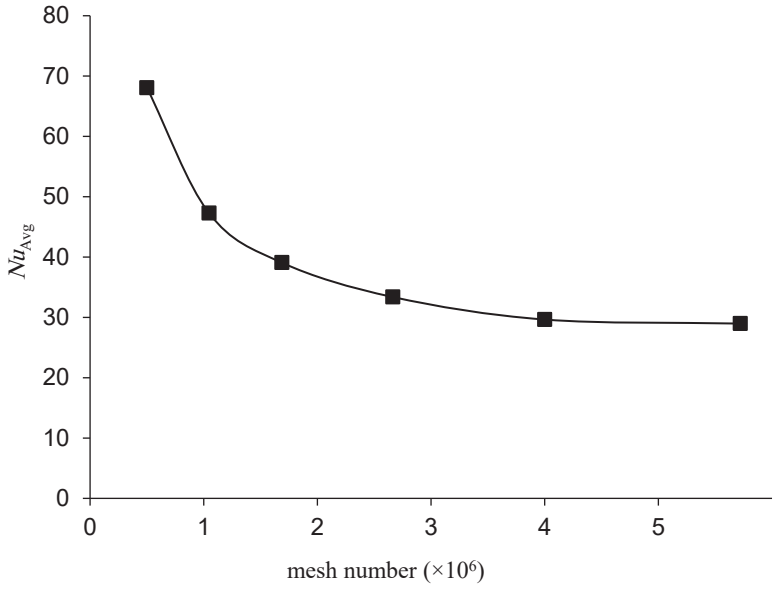

Fig. 2. Grid independence study at Ra=10^8 , $\phi_m = 0.04$ **and** mnf=5.67×10^{10}

2- 4- Thermophysical properties of ferrofluid

Density, specific heat, volumetric expansion coefficient, thermal conductivity, and viscosity of ferrofluid are computed as follows [43-45]:

$$\rho_{nf} = (1-\phi)\rho_f + \phi\rho_p \tag{17}$$

$$(\rho c_p)_{nf} = (1-\phi)(\rho c_p)_f + \phi(\rho c_p)_p \tag{18}$$

$$(\rho\beta)_{nf} = (1-\phi)(\rho\beta)_f + \phi(\rho\beta)_p \tag{19}$$

$$k_{nf} = \frac{k_p + 2k_f - 2\phi(k_p - k_f)}{k_p + 2k_f + 2\phi(k_p - k_f)} k_f \tag{20}$$

$$\mu_{nf} = \frac{\mu_f}{1-34.87(\frac{d_p}{d_f})^{-0.3}\phi^{1.03}} \tag{21}$$

In Eq. (17-21) the subscripts '*p*', '*f*', and '*nf*' stand for the properties of the nanoparticle, base fluid (water), and nanofluid, respectively. Table 2 presents the thermophysical properties of both phases used in this work.

2- 5- Computational methodology and mesh independence

The open-source and the finite volume-based code (*OpenFOAM 2.3.1*) is used to solve the governing equations. New solvers are developed in *OpenFOAM* to model the two-phase thermomagnetic convection of ferrofluid. Transient simulations are performed by the *PISO* algorithm. The Central difference and upwind schemes are employed to discretize the diffusion and convection terms with the second-order Crank-Nicolson for temporal discretization [46]. An iterative approach is utilized to solve the algebraic equations. The mesh

independence study is performed for $\mathrm{Ra}=10^8$, $\phi_m = 0.04$ and $\mathrm{mnf}=5.67\times10^{10}$. The average Nusselt number is obtained for six different meshes with grid points of $100\times100\times50$, $125\times125\times67$, $150\times150\times75$, $175\times175\times87$, $200\times200\times100$, and $225\times225\times113$. As shown in Fig. 2, the results become grid-independent for grid resolution of $200\times200\times100$ and therefore, this mesh is used for all computations. Non-uniform grid layouts are used in the *x* and *y*-directions. It should be mentioned that the normal distances between the first cell centers and the wall in the viscous unit are $\Delta y^+ = \Delta y.u_\tau / v \approx 0.4$ and $\Delta x^+ = \Delta x.u_\tau / v \approx 0.2$. Also a grid growth factor of 1.16 is applied both in the *x* and *y* directions. However, a uniform grid is employed in the *z*-direction where the corresponding grid spacing in the viscous unit is $\Delta z^+ = \Delta z.u_\tau / v \approx 1.1$.

2- 6- Proper Orthogonal Decomposition

To investigate the impact of a non-uniform magnetic field on turbulent flow, it is essential to analyze coherent structures. Identifying coherent structures in complex flows is crucial for understanding the underlying physics. Various methods can be used for identification, such as the *Q* criterion, *λ2* criterion [47], or coherent vortex extraction [48]. One widely used method is the proper orthogonal decomposition (POD) [49], which is a linear decomposition technique. It provides a set of optimal spatial empirical eigenfunctions that are orthonormal. The POD captures the maximum amount of energy possible for a given number of modes. This unique characteristic of the POD allows us to not only gain insights into different fluid structures present in a collection of events but also sort them based on their average energy content when the eigenfunctions are projected onto the original database.

The POD method seeks spatial basis functions that capture the most energetic components of a dynamic system. In the context of a numerical simulation, we have recorded *N* snapshots of the three-dimensional velocity and pressure fluctuation field. The POD technique then decomposes the fluctuating velocity into a collection of spatial modes, each associated with temporal coefficients. These spatial modes represent the dominant patterns or structures in the velocity field, while the temporal coefficients describe how these modes vary over time.

In the present numerical work, the Proper Orthogonal Decomposition algorithm has been utilized. At every time step, the velocity fluctuations can be obtained by subtracting the average velocity from the instantaneous velocity. The inner product in the Hilbert space is given by

$$\mathbf{C}_{ij} = \frac{1}{N}\int_{\Omega} u'(\vec{\mathbf{X}},t_i^*)u'(\vec{\mathbf{X}},t_j^*)d\Omega\ddot{\mathbf{x}} \tag{22}$$

where $i,j = 1,2,...,N$ represents the number of Snapshots, $\vec{\mathbf{X}}$ denotes the dimensionless position vector, and $d\Omega$ is a volume element. Eigenvalues and eigenvectors can be obtained by the Singular Value Decomposition (SVD) of the **C**-tensor.

$$\mathbf{CA} = \boldsymbol{\lambda}\mathbf{A} \tag{23}$$

In Eq. (22), $\boldsymbol{\lambda}$ is the eigenvalue and **A** is the corresponding eigenvector. Eigenmodes of POD are then obtained using the velocity fluctuations field and eigenvectors:

$$\boldsymbol{\lambda}_{ij}(\vec{\mathbf{X}}) = \sum_{i=1}^{N}\mathbf{A}_{ki}F'(\vec{\mathbf{X}},t_j^*) \tag{24}$$

where *k* represents the eigenmode number. The total energy of the fluctuations is determined from the sum of eigenvalues:

$$E = \sum_{i=1}^{N}\boldsymbol{\lambda}_i \tag{25}$$

where N is the mode number.

In addition, the energy ratio of the n-th mode to the total energy (or relative energy) is obtained from

$$\boldsymbol{\xi}_n = \boldsymbol{\lambda}_n / E \tag{26}$$

Also, the sum of the cumulative energy of the first *N* mode is calculated from

$$\boldsymbol{\xi}_n = \sum_{i=1}^{N}\boldsymbol{\lambda}_i / E \tag{27}$$

2- 7- Validation

In the present work, a new solver is developed in openFoam open source code for two-phase, turbulent free convection magnetic nanofluid flow under the effect of the nonuniform magnetic field. To the best of the author's knowledge, there are no experimental or numerical results that include all the cases in the literature, therefore, in this section, the validation of each part of the developed code is discussed separately. For validation of different parts of the developed code, several comparisons are conducted with the available literature. For validation of the two-phase modeling part of the developed code, the average Nusselt number values for two-phase free convection of $\mathrm{Al_2O_3}$/Water nanofluid within a square enclosure are compared in Fig. 3 (a) (for $\phi_{Ave} = 0.03$, $Pr = 4.623$, $d_p = 33\mathrm{nm}$ and $3.37\times10^5 \le Ra \le 1.68\times10^6$). Acceptable accordance is seen between the reported data in [50, 51] and present predictions.

Furthermore, to check the validity of the non-uniform magnetic field effect modeling part of the code, current numerical results are compared with the ones reported by Song and Tagawa [52] for thermomagnetic convection of gaseous oxygen gas within a square cavity for $B_r = 2\mathrm{T}$ and

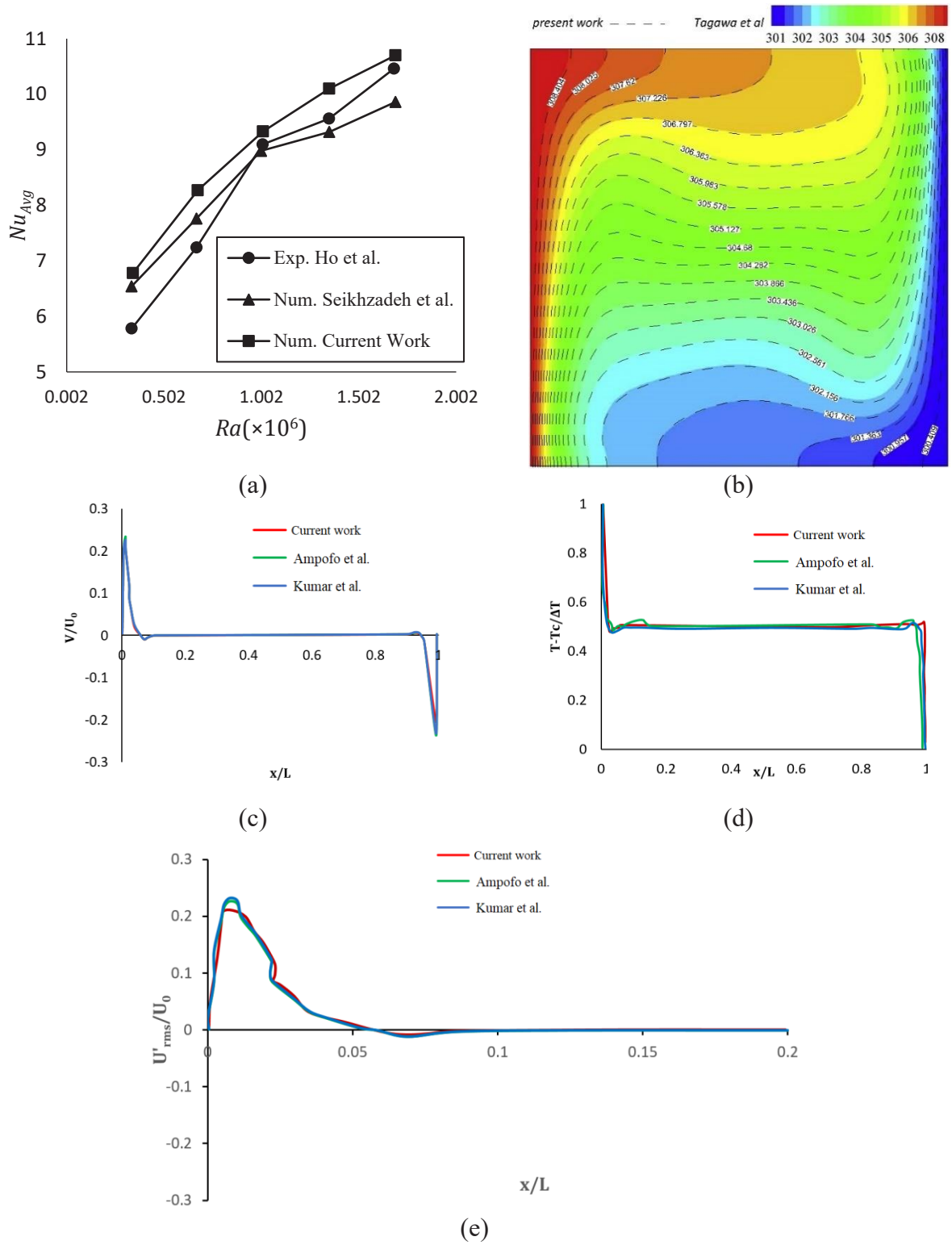

Fig. 3. (a) The mean Nusselt number as a function of Ra [50, 51] (b) Comparison of temperature fields [52] (c) The distribution of the time-averaged vertical velocity [53, 54] (d) The distribution of temperature along the horozintal midline [53, 54] (e) Comparison of root mean square (RMS) of fluctuations of horizontal velocity near the hot wall [53, 54].

$x_m / L = 0.6$. Comparison of temperature field is illustrated in Fig. 3 (b). It is evidence that the current code has good agreement with the results of [52].

Moreover, in Fig. 3 (c), (d), and (e) the distribution of the time-averaged vertical velocity (d) The distribution of temperature along the horizontal midline (e) the Comparison of RMS fluctuations of horizontal velocity near the hot wall.

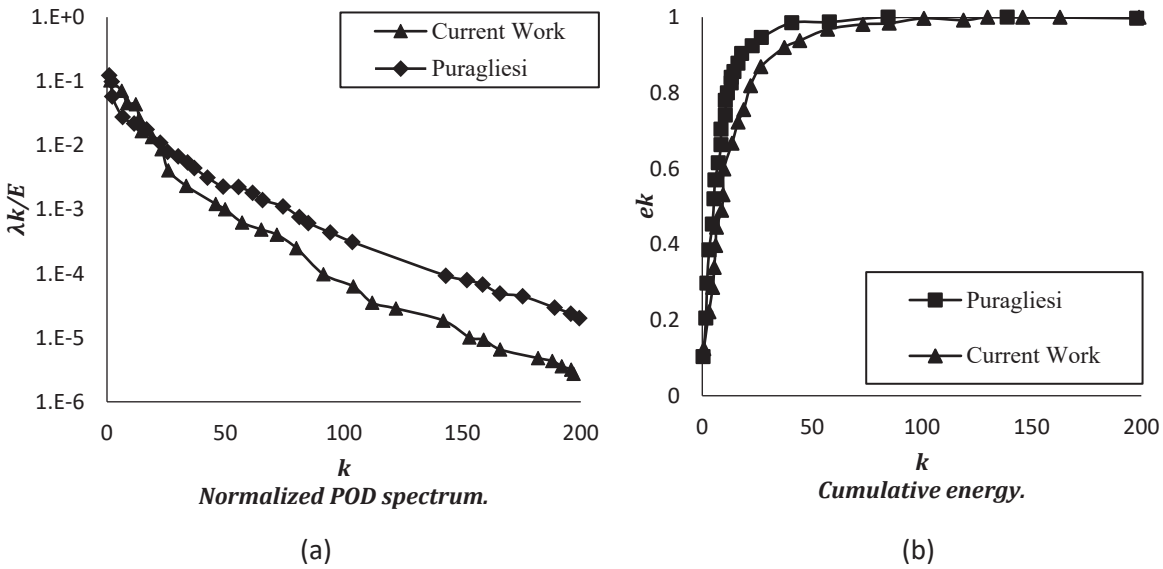

Fig. 4. Comparison of the current results with the reported data of Puragliesi et al. [55](a) Relative energy (b) Cumulative energy

Ampofo et al. [53] conducted experimental investigations, while Kumar et al. [54] performed numerical studies on turbulent free convection in a cubic enclosure under specific conditions ($Ra = 1.58\times10^{9}$ and $Pr = 0.71$). These studies involved making further comparisons. It can be seen that time-averaged vertical velocity and temperature profiles at the horizontal midline and also RMS fluctuations of horizontal velocity near the hot wall are in good agreement with published results. Finally, to verify the extraction of coherent structures and their energy, present outcomes are compared with the DNS results of Puragliesi et al. [55]. The comparison is plotted in Fig. 4. The current results are seen to agree quite well with the ones reported by Puragliesi et al. [55].

3- Results and Discussion

The primary objective of the present work is to conduct a Large-Eddy Simulation (LES) of two-phase turbulent thermo-magnetic convection of a ferrofluid inside a cubic cavity. The study focuses on investigating various aspects, including the mean Nusselt number and coherent structures of the first three modes for *x*-velocity, *y*-velocity, and pressure fluctuations. Additionally, non-dimensional relative energy and cumulative relative energy analyses are performed for each mode under different magnetic number values, specifically $mnf = 0$, 1.4×10^{10} and 5.6×10^{10}. It is worth noting that the numerical computations consistently maintain the particle volume fraction and Rayleigh values at 0.04 and 10^{8}, respectively, throughout the study.

Table 3 presents the mean Nusselt number values corresponding to different magnetic numbers. The results indicate that the presence of a magnetic field leads to an increase in heat transfer. Specifically, at magnetic numbers of 1.4×10^{10} and 5.6×10^{10}, an increase of 8.71% and 16.67% in the Nusselt number is observed, respectively. This enhancement in heat transfer is likely attributed to the influence of the Kelvin force resulting from the non-uniform magnetic field, which also impacts the coherent structures of the turbulent flow. Consequently, the subsequent sections of the article will delve into the changes induced in the coherent structures through the application of the magnetic field. The variables analyzed using this approach include velocity fluctuations in the *x*-direction (u'), velocity fluctuations in the *y*-direction (v'), and pressure fluctuations (p').

3- 1- Decomposition of orthogonal modes of x-velocity fluctuations

We first apply the algorithm for separating orthogonal modes for the velocity fluctuation in the *x*-direction (u'), which can be obtained by subtracting the average velocity from the instantaneous velocity. It is necessary to show that the results are independent of time and the number of snapshots. As illustrated in Fig. 5, as the number of snapshots grows, the value of relative energy or energy ratio of the first mode ($\xi_1 = \lambda_1 / E$) decreases and after 76 snapshots it approximately remains constant. Therefore, in this study, 76 snapshots are used in all cases.

In all cases, the runs lasted for 300 seconds. Data is saved every 4 seconds to apply POD method. As a result, the POD method has been applied to 75 snapshots.

Fig. 6 shows the cumulative and relative energies of modes for different magnetic numbers.

Table 3. Average Nu number (N_{uave}) on walls of the cavity at $Ra = 10^8$, and different magnetic numbers ($\phi_m = 0.04$)

mnf	0	1.4×10^{10}	5.6×10^{10}
Nu_{Avg}	24.11	26.21	28.13

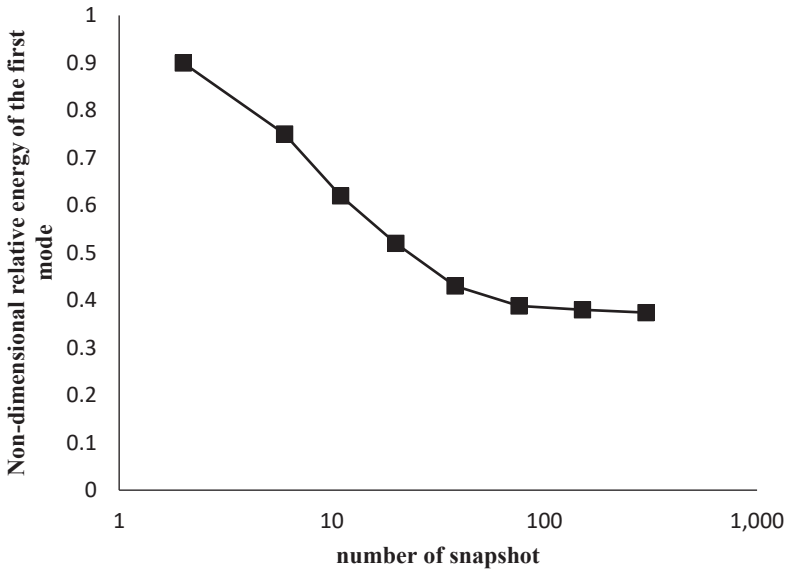

Fig. 5. Non-dimensional relative energy or energy ratio for the first mode as a function of the number of snapshots at Rayleigh $Ra = 10^8$, $mnf = 5.6\times10^{10}$ and .

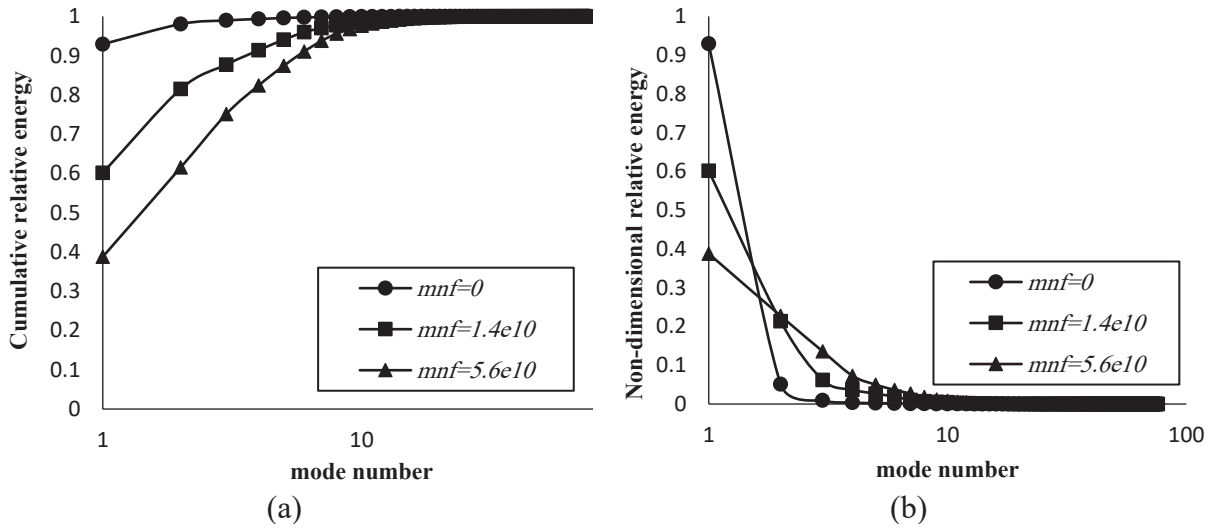

Fig. 6. The relative energy or energy ratio of modes for different magnetic numbers (a) cumulative (b) individual (for x-velocity fluctuations)

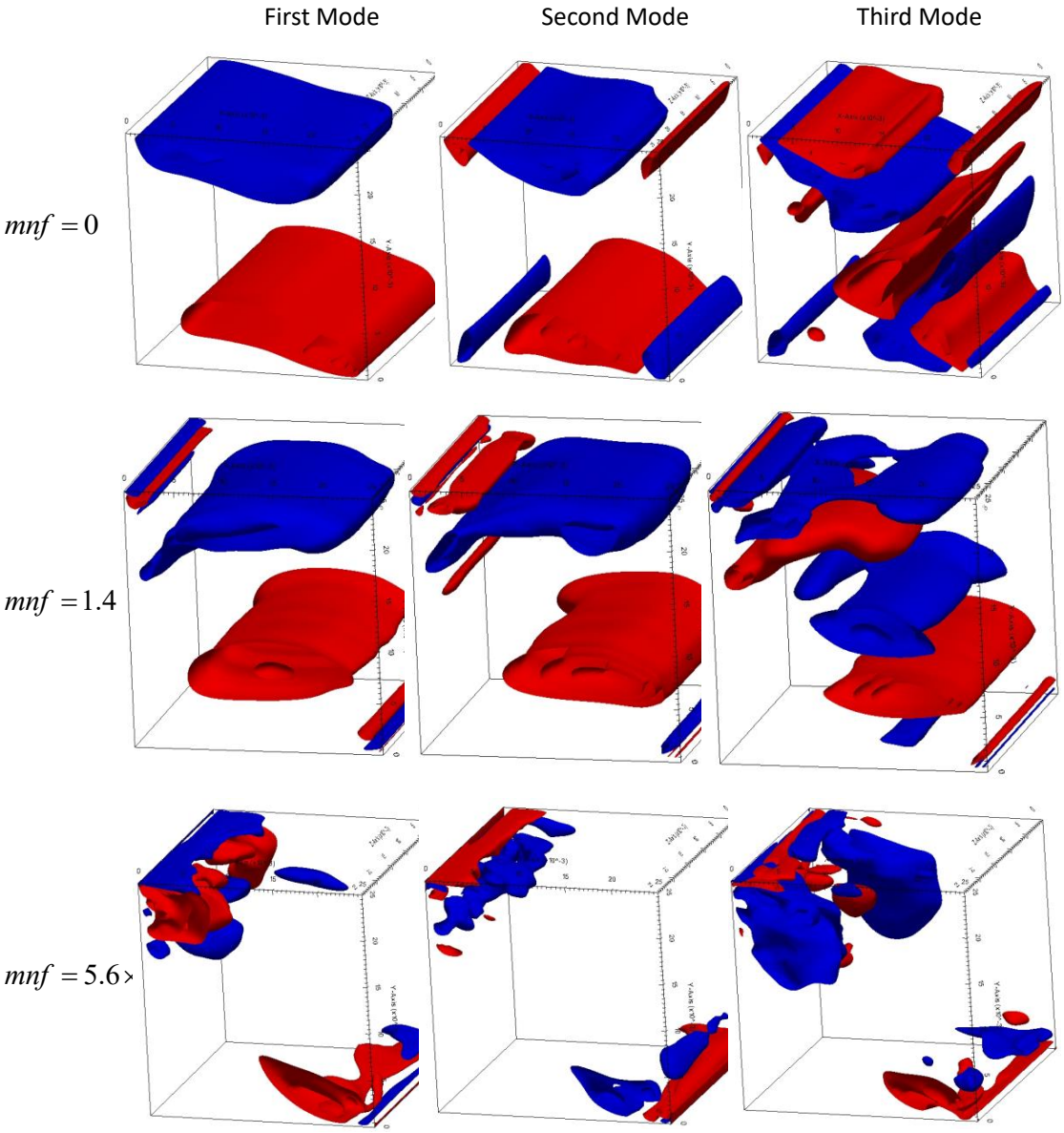

Fig. 7. Coherent structures of the first three modes for different magnetic numbers for x-velocity fluctuations

According to Fig. 6 (a), the cumulative energy is reduced by increasing the magnetic number. It is found that the number of modes required to reconstruct 98% of the flow energy is 2, 8, and 10 for $mnf = 0$, $mnf = 1.4 \times 10^{10}$ and $mnf = 5.6 \times 10^{10}$, respectively. Hence, the dynamics can be completely understood from the analysis of these modes. Similar conclusions have also been drawn by Feng et al. [56] where they observed that the first few modes dominate the global flow field. From the results, employing the magnetic field increases the number of turbulent scales and coherent structures. As seen in Fig. 6 (b), as the magnetic number increases the relative energy of the first mode reduces while that of the other modes increases. Therefore, it can be concluded that the increase in heat transfer due to the increase in the magnetic number which can be seen in Table 4 can be Since by applying the magnetic field new eddies with high energy are created in the flow, and they play a positive role in the heat transfer process. To study the shape of these new structures, the shape of modes containing energy is drawn and analyzed.

Fig. 7 shows the first three modes for different magnetic numbers extracted by the POD algorithm. According to Fig. 7, the first mode for $mnf = 0$ has a plane structure (parallel to the *xz*-plane) with an energy ratio of 93% which covers the areas close to the bottom and top walls of the enclosure. Buoyancy forces are responsible for these structures. Due to the high relative energy of the first mode, the hydrodynamics of the flow is almost affected by the first mode. The second mode for $mnf = 0$, contains only 5% of the relative energy of the flow which is much lower than that of the first mode.

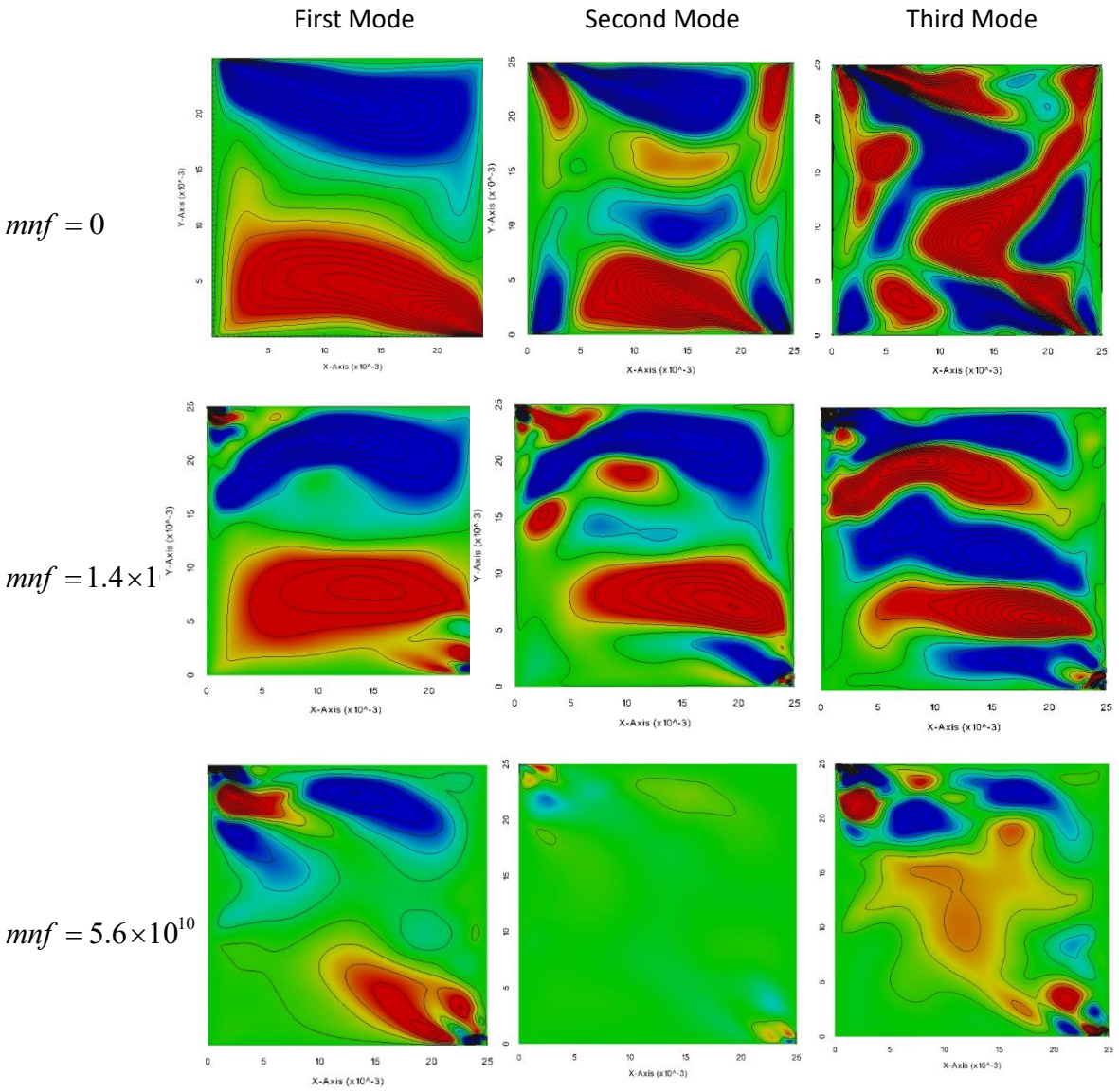

Fig. 8. 2D representation of coherent structures for the first three modes in the vertical mid-plane of the enclosure at different magnetic numbers for x-velocity fluctuations.

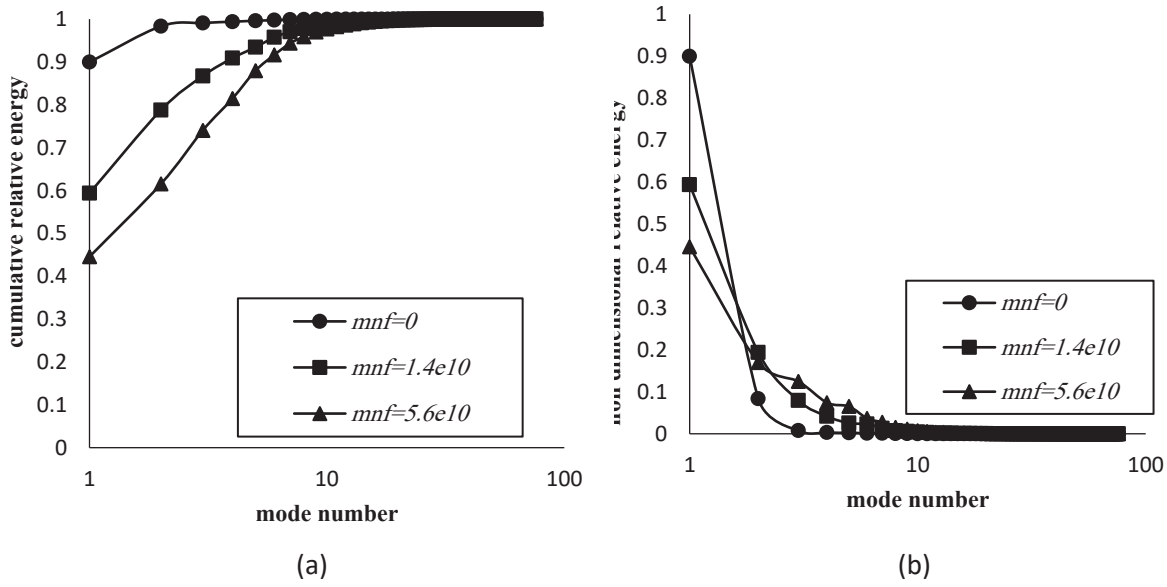

Fig. 9. The relative energy of modes for different magnetic numbers (a) cumulative (b) individual (for y-velocity fluctuations)

According to Fig. 7, it is observed that in the second mode, the plane coherent structures are still formed in the cavity. However, these structures are not as large as the first mode. This is the main reason for the decrease in the relative energy of the second mode compared to the first mode. Additionally, there are some other small coherent structures near the plane structures. The relative energy of the third mode is only about 0.9%. As shown, the structures of the third mode are small, complex, and irregular. Consequently, the third mode does not have any appreciable effect on the turbulence mechanism. For $mnf = 1.4\times10^{10}$, the relative energy values of the first, second, and third modes are 60%, 21%, and 6%, respectively. With exerting magnetic field, the energy of the first mode is decreased significantly, but for other modes, the relative energy becomes higher than that of $mnf = 0$. It can be seen that for $mnf = 1.4\times10^{10}$, in addition to plane structures, the span-wise roll structures are formed near the magnetic sources because of magnetic body forces. For $mnf = 5.6\times10^{10}$, the relative energy of the first mode is 39% which is lower than of corresponding value for $mnf = 1.4\times10^{10}$. It can be observed that by employing a strong magnetic field, the plane structures of buoyancy forces disappear and only the span-wise roll structures due to Kelvin's body forces are created. It can be concluded that the applied magnetic field reduces the relative energy of the first mode. On the other hand, the energies of other modes are increased by the applied magnetic field.

For better representation, 2D plots of coherent structures of the first three modes in the vertical mid-plane of the enclosure and at various magnetic numbers are illustrated in Fig. 8. As seen in Fig. 8, in the absence of magnetic field ($mnf = 0$), the flow pattern is composed of plane structures arising from buoyant effects. For a moderate magnetic field ($mnf = 1.4\times10^{10}$), on the other hand, coherent structures are a combination of plane and span-wise roll structures. However, at high magnetic fields, the coherent structures are governed by span-wise roll ones as a result of the vigorous magnetic forces. It is observed that the first three modes (leading modes) play a dominant role in the sweeping and ejection of large-scale structures as stated in {Feng, 2011 #13}. In contrast, the remaining POD modes are weaker as each of them represents less than 2% of the total turbulent kinetic energy. If the magnetic number is increased, the first four modes would capture less kinetic energy. The reason is that more small-scale turbulent structures appear in the flow field with increasing magnetic number, and these fine scale structures also have a contribution to the energy content, which means that the relative contribution of the large-scale structures decreases.

3- 2- Decomposition of orthogonal modes of y-velocity fluctuations

Fig. 9 illustrates the cumulative and individual energies of modes for different magnetic numbers.

The general trends are similar to those presented for the *x*-velocity fluctuations. Once again, it can be observed that the applied magnetic field decreases the cumulative energy. Besides, the applied magnetic field declines the relative energy of the first mode but enhances that of other modes.

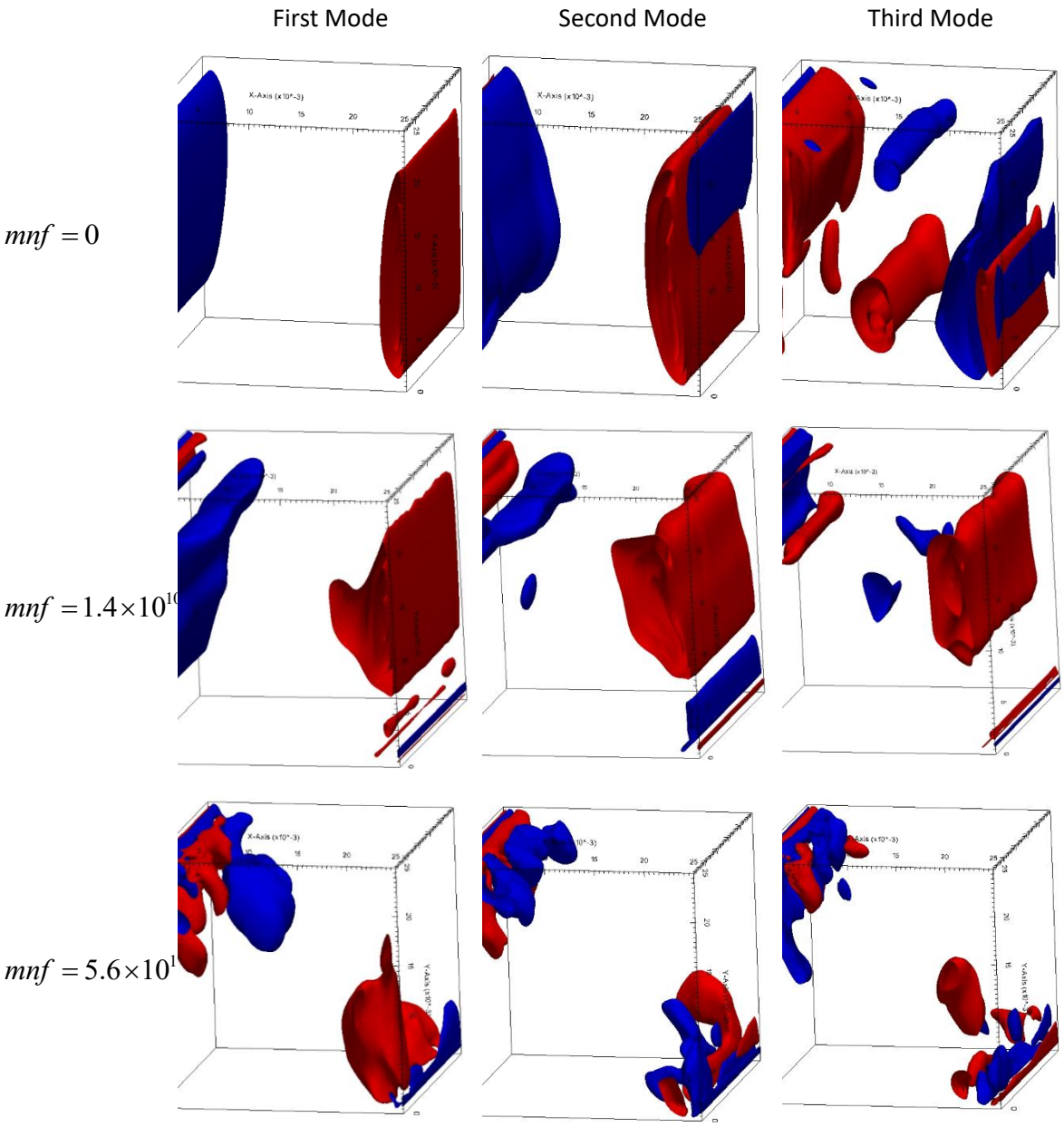

Fig. 10. Coherent structures of the first three modes for different magnetic numbers for y-velocity fluctuations

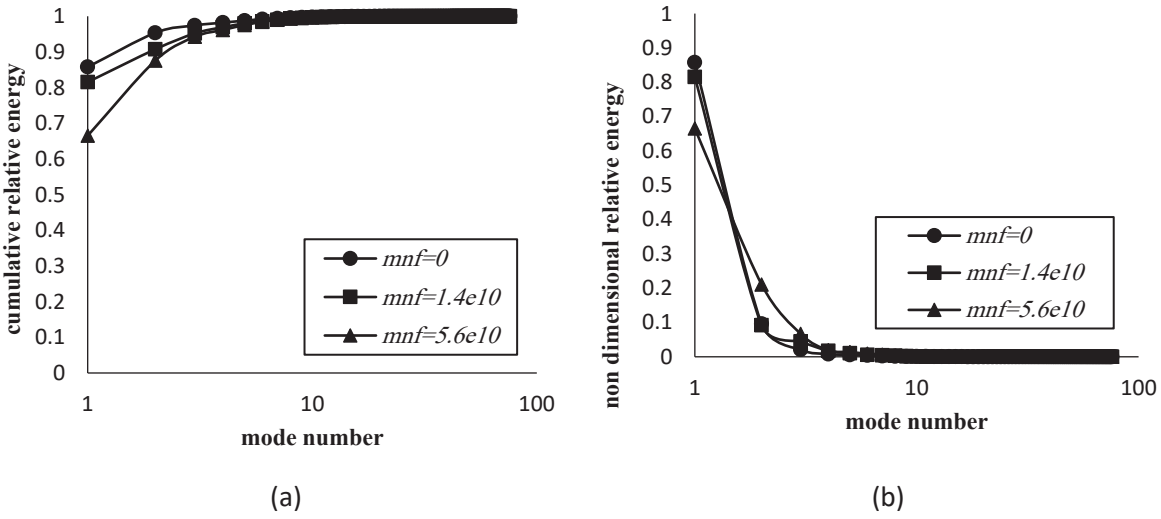

(a) (b)

Fig. 11. The relative energy of modes for different magnetic numbers (a) cumulative (b) individual (for pressure fluctuations)

Fig. 10 depicts the first three modes for various magnetic numbers. For buoyant flow ($mnf = 0$), it is found that the relative energies of the first, second, and third modes are about 89, 9, and 0.7%, respectively. As shown, the coherent structure of the first mode of buoyant flow has a plane shape (parallel to the *yz*-plane) which is located near the vertical walls. By employing a magnetic field with an intensity of $mnf = 1.4\times10^{10}$, the relative energy of the first mode is decreased to 59% whereas, the energies of the second and third modes are increased to 19%, and 9%, respectively. For $mnf = 1.4\times10^{10}$, both plane and span-wise roll structures exist as a result of buoyancy and magnetic forces, respectively. For the highest magnetic field intensity i.e. $mnf = 5.6\times10^{10}$ the values of the first, second, and third modes are found to be 44%, 17%, and 12%, respectively. In this case, the flow structures that are span-wise rolls are completely controlled by magnetic forces. It is seen, that with increasing the mode number the structures get a more irregular shape.

3- 3- Decomposition of orthogonal modes of pressure fluctuations

Fig. 11 (a) and Fig. 11 (b) show the cumulative and relative energy of modes, respectively. Similar to what was seen for *x* and *y*-velocity fluctuations, the relative energy value of the first mode decreases by the magnetic field. On the contrary, the relative energy values of higher modes are increased by increasing magnetic numbers.

Fig. 12 shows the influence of the magnetic field on the first three modes. Generally, the structures are quite similar for $mnf = 0$ and $mnf = 1.4\times10^{10}$. In the case of $mnf = 1.4\times10^{10}$, both plane and roll structures exist simultaneously. The plane structures diminish at $mnf = 5.6\times10^{10}$ due to dominant magnetic forces thereby coherent structures are governed by the magnetic field.

Fig. 13 shows the time coefficients of the first, second, and third modes at different magnetic numbers. As seen, regardless of the magnetic number, the values of the time coefficients of the first mode are higher than that of the other modes, implying the dominance of the first mode in the turbulence structures. It is worth noting that regardless of the mode number, the values of time coefficients increase with enhancing magnetic number.

4- Conclusion

To conduct a numerical study of coherent structures in turbulent flows, it is crucial to employ a method capable of resolving flow eddies within the computational domain. The chosen method should be able to accurately capture and represent the intricate details of these eddies. Understanding the impact of various parameters on turbulence and its structures requires effective visualization of the coherent structures. By visualizing these structures, researchers can gain insights into the characteristics and behavior of turbulent flow, allowing for a deeper understanding of the underlying dynamics. In this study, the turbulent flow of free convection in a magnetic nanofluid subjected to a non-uniform magnetic field was modeled using a large eddy simulation. An important aspect of this work was to explore, for the first time, the influence of the Kelvin force resulting from the magnetic field on the coherent structures present in this type of turbulent flow. To achieve this, the proper orthogonal decomposition (POD) method was employed to reveal and analyze these coherent structures. By utilizing the POD technique, the flow was decomposed into a set of empirical eigenfunctions that are linearly independent, providing insights into the spatial coherent structures of the flow. This approach allowed for a deeper understanding of the behavior and characteristics of the coherent structures in the turbulent flow of the magnetic nanofluid under the influence of the non-uniform magnetic field.

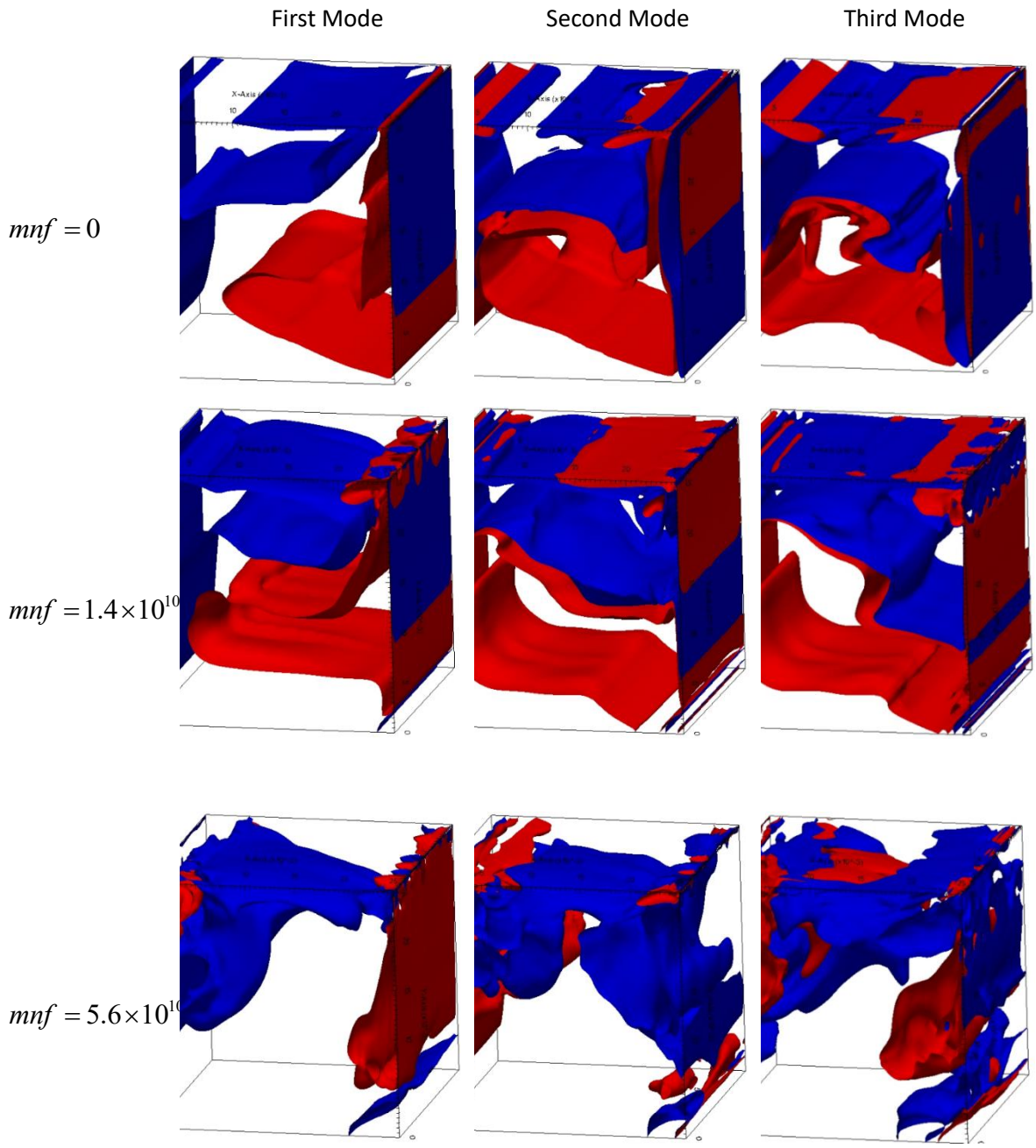

Fig. 12. Coherent structures of the first three modes for different magnetic numbers for pressure fluctuations

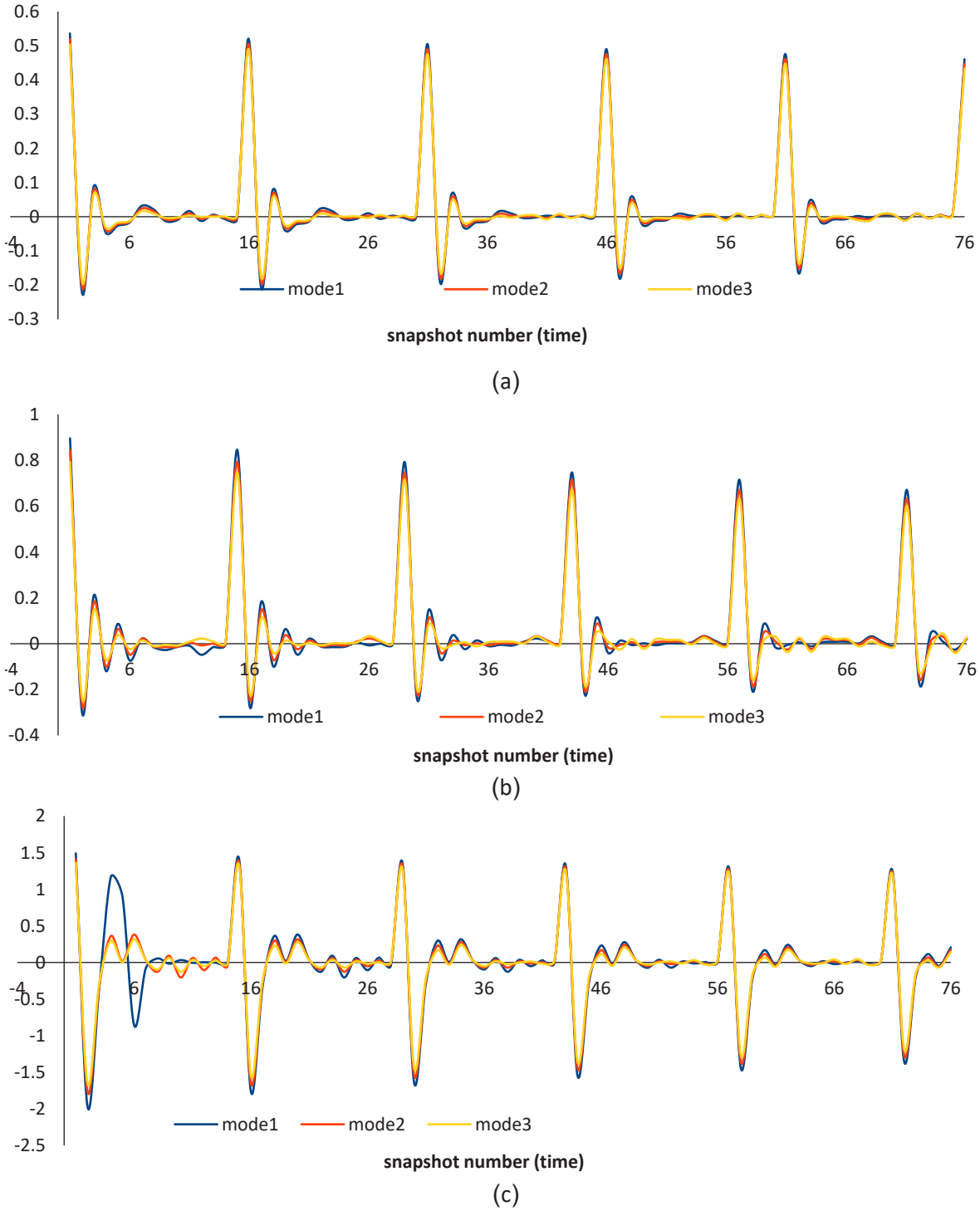

Fig. 13. The time coefficients of the first three modes of pressure fluctuations for different magnetic numbers (a) $mnf = 0$ **(b)** $mnf = 1.4 \times 10^{10}$ **(c)** $mnf = 5.6 \times 10^{10}$

The main outcomes of the present work can be summarized as:

In Rayleigh number 10^8 and a volume fraction of 4%, increasing the magnetic number from 0 to $mnf = 1.4\times10^{10}$ and $mnf = 5.6\times10^{10}$ results in an increase of 8.71% and 16.67%, respectively.

With an increase in the magnetic number from 0 to $mnf = 1.4\times10^{10}$ and $mnf = 5.6\times10^{10}$, the number of coherent structures associated with the oscillatory component of velocity fluctuation in the x-direction increases from 2 to 8 and 10, respectively.

The relative energy of the first mode is declined by increasing the magnetic number.

The relative energy of the higher modes grows as the magnetic number is enhanced.

The cumulative energies of modes decrease as the magnetic number increases.

The coherent structures are converted from the plane-shaped to the span-wise roll structures at high magnetic numbers.

Irrespective of the mode number, the time coefficients are increased by increasing the magnetic number.

Understanding the nature of coherent structures and their response to the applied magnetic field can provide insights for controlling the main flow dynamics. The findings highlight the potential for improved heat transfer through the manipulation of coherent structures in two-phase turbulent thermo-magnetic convection.

Nomenclature

$\mathbf{A}$	Eigenvector, [-]
D_B	Brownian diffusivity, [m^2 s^{-1}]
D_T	Thermophoresis diffusivity, [m^2 s^{-1}]
D_t	Eddy diffusivity, [m^2 s^{-1}]
d_p	Diameter of particles, [nm]
Ec	Ecker number, [-]
$\vec{\mathbf{H}}$	Intensity of magnetic field, [A m^{-1}]
L	Side length of cavity, [m]
Le	Lewis number, [-]
$L(\zeta)$	Langevin function, [-]
I	Electrical current, [A]
$\vec{\mathbf{J}}$	Flux vector of particles, [kg m^{-2} s^{-1}]
k	Thermal conductivity, [W m^{-1} K^{-1}]
k_B	Boltzmann's constant (=1.38066×10^{-23}), [J K^{-1}]
M	Magnetization, [A/m]
mnf	Magnetic number, [-]
Ms	Saturation magnetization, [A/m]
m_p	Magnetic moment, [A m^2]
Nu	Nusselt number, [-]
p	Pressure, [Pa]
Pr	Prandtl number, [-]
Ra	Rayleigh number, [-]
Sc	Schmidt number, [-]
T	Temperature, [K]
$\vec{\mathbf{V}}$	Velocity vector, [m s^{-1}]

Greek symbols

α	Thermal diffusivity, [m^2 s^{-1}]
β	Volumetric expansion coefficient, [K^{-1}]
μ_0	Vacuum permeability, [T.m A^{-1}]
μ_B	Bohr magneton, [A m^2]
ρ	Density, [kg m^{-3}]
φ	Void fraction, [-]

Subscripts

f	Base fluid
p	Particle
nf	Nanofluid
o	Reference state

References

[1] O. Oehlsen, S.I. Cervantes-Ramírez, P. Cervantes-Avilés, I.A. Medina-Velo, Approaches on ferrofluid synthesis and applications: current status and future perspectives, ACS omega, 7(4) (2022) 3134-3150.

[2] R.E. Rosensweig, Ferrohydrodynamics, Courier Corporation, 2013.

[3] H. Aminfar, M. Mohammadpourfard, Y.N. Kahnamouei, A 3D numerical simulation of mixed convection of a magnetic nanofluid in the presence of non-uniform magnetic field in a vertical tube using two phase mixture model, Journal of Magnetism and Magnetic Materials, 323(15) (2011) 1963-1972.

[4] H. Aminfar, M. Mohammadpourfard, S.A. Zonouzi, Numerical study of the ferrofluid flow and heat transfer through a rectangular duct in the presence of a non-uniform transverse magnetic field, Journal of Magnetism and Magnetic materials, 327 (2013) 31-42.

[5] M. Sheikholeslami, M. Seyednezhad, Nanofluid heat transfer in a permeable enclosure in presence of variable magnetic field by means of CVFEM, International

Journal of Heat and Mass Transfer, 114 (2017) 1169-1180.

[6] M. Mohammadpourfard, H. Aminfar, S. Ahangar Zonouzi, Numerical investigation of the magnetic field effects on the entropy generation and heat transfer in a nanofluid filled cavity with natural convection, Heat Transfer—Asian Research, 46(5) (2017) 409-433.

[7] G. Ashwinkumar, C. Sulochana, S. Samrat, Effect of the aligned magnetic field on the boundary layer analysis of magnetic-nanofluid over a semi-infinite vertical plate with ferrous nanoparticles, Multidiscipline Modeling in Materials and Structures, 14(3) (2018) 497-515.

[8] M.B. Gerdroodbary, M. Sheikholeslami, S.V. Mousavi, A. Anazadehsayed, R. Moradi, The influence of non-uniform magnetic field on heat transfer intensification of ferrofluid inside a T-junction, Chemical Engineering and Processing-Process Intensification, 123 (2018) 58-66.

[9] A. Khosravi, M. Malekan, M.E. Assad, Numerical analysis of magnetic field effects on the heat transfer enhancement in ferrofluids for a parabolic trough solar collector, Renewable Energy, 134 (2019) 54-63.

[10] P.S. Szabo, W.-G. Früh, The transition from natural convection to thermomagnetic convection of a magnetic fluid in a non-uniform magnetic field, Journal of Magnetism and Magnetic Materials, 447 (2018) 116-123.

[11] T. Javed, M.A. Siddiqui, Effect of MHD on heat transfer through ferrofluid inside a square cavity containing obstacle/heat source, International Journal of Thermal Sciences, 125 (2018) 419-427.

[12] W. Wrobel, E. Fornalik-Wajs, J. Szmyd, Experimental and numerical analysis of thermo-magnetic convection in a vertical annular enclosure, International Journal of Heat and Fluid Flow, 31(6) (2010) 1019-1031.

[13] M. Lee, Y.-J. Kim, Effect of non-uniform magnetic fields on the characteristics of ferrofluid flow in a square enclosure, Journal of Magnetism and Magnetic Materials, 506 (2020) 166697.

[14] S.Y. Motlagh, E. Golab, A.N. Sadr, Two-phase modeling of the free convection of nanofluid inside the inclined porous semi-annulus enclosure, International Journal of Mechanical Sciences, 164 (2019) 105183.

[15] H. Soltanipour, A. Gharegöz, M.B. Oskooee, Numerical study of magnetic field effect on the ferrofluid forced convection and entropy generation in a curved pipe, Journal of the Brazilian Society of Mechanical Sciences and Engineering, 42(3) (2020) 135.

[16] S. Banik, A.S. Mirja, N. Biswas, R. Ganguly, Entropy analysis during heat dissipation via thermomagnetic convection in a ferrofluid-filled enclosure, International Communications in Heat and Mass Transfer, 138 (2022) 106323.

[17] K. Ayoubi Ayoubloo, S. Yazdani, M. Sheremet, O. Younis, M. Ghalambaz, Ferro-hydrodynamic induced convection flow and heat transfer of nanofluids in a corrugated wall enclosure, Journal of Taibah University for Science, 17(1) (2023) 2215675.

[18] B. Iftikhar, M.A. Siddiqui, T. Javed, Computational analysis of heat transfer via heatlines for MHD natural convection ferrofluid flow inside the U-shaped cavity, The European Physical Journal Plus, 138(2) (2023) 164.

[19] L. Shi, W. Tao, N. Zheng, T. Zhou, Z. Sun, Numerical study of convective heat transfer and particle distribution subject to magneto-static field in a square cavity, International Journal of Thermal Sciences, 185 (2023) 108081.

[20] D.D. Dixit, A. Pattamatta, Effect of uniform external magnetic-field on natural convection heat transfer in a cubical cavity filled with magnetic nano-dispersion, International Journal of Heat and Mass Transfer, 146 (2020) 118828.

[21] M. Goodarzi, M. Safaei, K. Vafai, G. Ahmadi, M. Dahari, S. Kazi, N. Jomhari, Investigation of nanofluid mixed convection in a shallow cavity using a two-phase mixture model, International Journal of Thermal Sciences, 75 (2014) 204-220.

[22] H. Abdi, S.Y. Motlagh, H. Soltanipour, Study of magnetic nanofluid flow in a square cavity under the magnetic field of a wire carrying the electric current in turbulence regime, Results in Physics, 18 (2020) 103224.

[23] H. Sajjadi, M. Beigzadeh Abbassi, G.R. Kefayati, Lattice Boltzmann simulation of turbulent natural convection in a square cavity using Cu/water nanofluid, Journal of Mechanical Science and Technology, 27 (2013) 2341-2349.

[24] A.K. Kareem, S. Gao, A comparison study of mixed convection heat transfer of turbulent nanofluid flow in a three-dimensional lid-driven enclosure with a clockwise versus an anticlockwise rotating cylinder, International Communications in Heat and Mass Transfer, 90 (2018) 44-55.

[25] Y. Cao, Y. Bai, J. Du, S. Rashidi, A computational fluid dynamics investigation on the effect of the angular velocities of hot and cold turbulator cylinders on the heat transfer characteristics of nanofluid flows within a porous cavity, Journal of Energy Resources Technology, 142(11) (2020) 112104.

[26] H. Ghodsinezhad, M. Sharifpur, J.P. Meyer, Experimental investigation on cavity flow natural convection of Al2O3–water nanofluids, International Communications in Heat and Mass Transfer, 76 (2016) 316-324.

[27] A.P. Patel, D. Bhatnagar, R.S. Kumar, S. Prabhu, Numerical study on turbulent natural convection and radiation heat transfer of nanofluids in a differentially heated square enclosure, Journal of Thermal Analysis and Calorimetry, (2020) 1-10.

[28] R. Harish, R. Sivakumar, Turbulent thermal convection of nanofluids in cubical enclosure using two-phase mixture model, International Journal of Mechanical Sciences, 190 (2021) 106033.

[29] R. Harish, R. Sivakumar, Effects of nanoparticle dispersion on turbulent mixed convection flows in cubical enclosure considering Brownian motion and thermophoresis, Powder Technology, 378 (2021) 303-316.

[30] E. Mignot, W. Brevis, Coherent turbulent structures within open-channel lateral cavities, Journal of Hydraulic Engineering, 146(2) (2020) 04019066.

[31] G. Janiga, Large-eddy simulation and 3D proper orthogonal decomposition of the hydrodynamics in a stirred tank, Chemical Engineering Science, 201 (2019) 132-144.

[32] P.S. Mahapatra, S. Chatterjee, A. Mukhopadhyay, N.K. Manna, K. Ghosh, Proper orthogonal decomposition of thermally-induced flow structure in an enclosure with alternately active localized heat sources, International Journal of Heat and Mass Transfer, 94 (2016) 373-379.

[33] B. Podvin, A. Sergent, Proper orthogonal decomposition investigation of turbulent Rayleigh-Bénard convection in a rectangular cavity, Physics of Fluids, 24(10) (2012).

[34] S.Y. Motlagh, S. Taghizadeh, POD analysis of low Reynolds turbulent porous channel flow, International Journal of Heat and Fluid Flow, 61 (2016) 665-676.

[35] E. Tzirtzilakis, M. Xenos, Biomagnetic fluid flow in a driven cavity, Meccanica, 48 (2013) 187-200.

[36] R.E. Rosensweig, Heating magnetic fluid with alternating magnetic field, Journal of magnetism and magnetic materials, 252 (2002) 370-374.

[37] J. Buongiorno, Convective Transport in Nanofluids, Journal of Heat Transfer, 128(3) (2005) 240-250.

[38] M.I. Shliomis, Convective Instability of Magnetized Ferrofluids: Influence of Magnetophoresis and Soret Effect, in: W. Köhler, S. Wiegand (Eds.) Thermal Nonequilibrium Phenomena in Fluid Mixtures, Springer Berlin Heidelberg, Berlin, Heidelberg, 2002, pp. 355-371.

[39] M.I. Shliomis, B.L. Smorodin, Convective instability of magnetized ferrofluids, Journal of Magnetism and Magnetic Materials, 252 (2002) 197-202.

[40] J. Smagorinsky, General circulation experiments with the primitive equations: I. The basic experiment, Monthly weather review, 91(3) (1963) 99-164.

[41] S.Y. Motlagh, H. Soltanipour, Natural convection of Al2O3-water nanofluid in an inclined cavity using Buongiorno's two-phase model, International Journal of Thermal Sciences, 111 (2017) 310-320.

[42] H. Soltanipour, Two-phase simulation of magnetic field effect on the ferrofluid forced convection in a pipe considering Brownian diffusion, thermophoresis, and magnetophoresis, The European Physical Journal Plus, 135(9) (2020) 1-23.

[43] B.C. Pak, Y.I. Cho, Hydrodynamic and heat transfer study of dispersed fluids with submicron metallic oxide particles, Experimental Heat Transfer an International Journal, 11(2) (1998) 151-170.

[44] Y. Xuan, W. Roetzel, Conceptions for heat transfer correlation of nanofluids, International Journal of heat and Mass transfer, 43(19) (2000) 3701-3707.

[45] J.C. Maxwell, A treatise on electricity and magnetism, Clarendon press, 1873.

[46] H. Weller, C. Greenshields, C. de Rouvray, The OpenFOAM Foundation Ltd, OpenFOAM. https:// openfoam. org, (2016).

[47] J. Jeong, F. Hussain, On the identification of a vortex, Journal of fluid mechanics, 285 (1995) 69-94.

[48] M. Farge, G. Pellegrino, K. Schneider, Coherent vortex extraction in 3D turbulent flows using orthogonal wavelets, Physical Review Letters, 87(5) (2001) 054501.

[49] J.L. Lumley, The structure of inhomogeneous turbulent flows, Atmospheric turbulence and radio wave propagation, (1967) 166-178.

[50] C. Ho, W. Liu, Y. Chang, C. Lin, Natural convection heat transfer of alumina-water nanofluid in vertical square enclosures: An experimental study, International Journal of Thermal Sciences, 49(8) (2010) 1345-1353.

[51] G.A. Sheikhzadeh, M. Dastmalchi, H. Khorasanizadeh, Effects of nanoparticles transport mechanisms on Al2O3–water nanofluid natural convection in a square enclosure, International Journal of Thermal Sciences, 66 (2013) 51-62.

[52] K.W. Song, T. Tagawa, Thermomagnetic convection of oxygen in a square enclosure under non-uniform magnetic field, International Journal of Thermal Sciences, 125 (2018) 52-65.

[53] F. Ampofo, T. Karayiannis, Experimental benchmark data for turbulent natural convection in an air filled square cavity, International Journal of Heat and Mass Transfer, 46(19) (2003) 3551-3572.

[54] R. Kumar, A. Dewan, A study of LES–SGS closure models applied to a square buoyant cavity, International Journal of Heat and Mass Transfer, 98 (2016) 164-175.

[55] R. Puragliesi, E. Leriche, Proper orthogonal decomposition of a fully confined cubical differentially heated cavity flow at Rayleigh number Ra= 109, Computers & fluids, 61 (2012) 14-20.

[56] L.-H. Feng, J.-J. Wang, C. Pan, Proper orthogonal decomposition analysis of vortex dynamics of a circular cylinder under synthetic jet control, Physics of Fluids, 23(1) (2011).

HOW TO CITE THIS ARTICLE

H. Abdi, S. Yekani Motlagh, H. Soltanipour, Large Eddy Simulation and Proper Orthogonal Decomposition Analysis of Two-phase Turbulent Thermomagnetic Convection of a Ferrofluid in a Cubic Cavity , AUT J. Mech Eng., 7(2) (2023) 155-174.

DOI: 10.22060/ajme.2023.22109.6054